

Unique Structural Features of Mule Deer Prion Protein Provide Insights into Chronic Wasting Disease

Urška Slapšak,[†] Giulia Salzano,[‡] Gregor Ilc,^{†,§} Gabriele Giachin,^{‡,||} Jifeng Bian,^{⊥,#} Glenn Telling,^{⊥,#} Giuseppe Legname,^{*,‡,||} and Janez Plavec^{*,†,§,∇}

[†]Slovenian NMR Centre, National Institute of Chemistry, SI-1000 Ljubljana, Ljubljana, Slovenia

[‡]Laboratory of Prion Biology, Department of Neuroscience, Scuola Internazionale Superiore di Studi Avanzati (SISSA), Via Bonomea 265, I-34136 Trieste, Trieste, Italy

[§]EN-FIST Centre of Excellence, SI-1000 Ljubljana, Ljubljana, Slovenia

^{||}Structural Biology Group, European Synchrotron Radiation Facility (ESRF), 38000 Grenoble, Auvergne-Rhône-Alpes, France

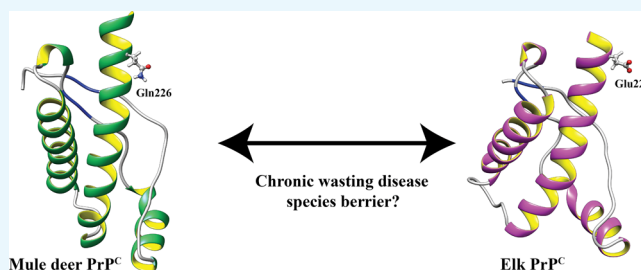
[⊥]Prion Research Center (PRC) and [#]Department of Microbiology, Immunology and Pathology, Colorado State University, Fort Collins, Colorado 80525, United States

^{||}ELETTRA-Sincrotrone Trieste S.C.p.A, 34149 Trieste, Friuli Venezia Giulia, Italy

[∇]Department of Chemistry and Biochemistry, Faculty of Chemistry and Chemical Technology, University of Ljubljana, SI-1000 Ljubljana, Ljubljana, Slovenia

Supporting Information

ABSTRACT: Chronic wasting disease (CWD) is a highly infectious prion disease of cervids. Accumulation of prions, the disease-specific structural conformers of the cellular prion protein (PrP^C), in the central nervous system, is the key pathological event of the disorder. The analysis of cervid PrP^C sequences revealed the existence of polymorphism at position 226, in which deer PrP contains glutamine (Q), whereas elk PrP contains glutamate (E). The effects of this polymorphism on CWD are still unknown. We determined the high-resolution nuclear magnetic resonance structure of the mule deer prion protein that was compared to previously published PrP structures of elk and white-tailed deer. We found that the polymorphism Q226E could influence the long-range intramolecular interactions and packing of the β 2– α 2 loop and the C-terminus of the α 3 helix of cervid PrP structures. This solvent-accessible epitope is believed to be involved in prion conversion. Additional differences were observed at the beginning of the well-defined C-terminus domain, in the α 2– α 3 region, and in its interactions with the α 1 helix. Here, we highlight the importance of the PrP structure in prion susceptibility and how single amino acid differences might influence the overall protein folding.



INTRODUCTION

Chronic wasting disease (CWD) is an infectious prion disease of free-ranging cervids. It has been reported in both captive and wild cervid species, including elk (*Cervus canadensis*), mule deer (*Odocoileus hemionus*), white-tailed deer (*Odocoileus virginianus*), red deer (*Cervus elaphus*), reindeer (*Rangifer tarandus*), and moose (*Alces alces*).^{1–7} The disease has now been reported in 26 states of the United States, three provinces of Canada, South Korea, Norway, Finland, and Sweden.^{7–12}

Prion diseases, also known as transmissible spongiform encephalopathies (TSEs), are rapid, progressive, and devastating neurodegenerative disorders, caused by misfolding events of the main α -helical cellular prion protein (PrP^C) to a β -sheet-enriched, partially protease-resistant, and infectious isoform (PrP^{Sc} or prion).^{13,14} Although there is a lack of high-resolution three-dimensional (3D) structural data for PrP^{Sc} (mostly because of its insolubility and propensity to

aggregate),¹⁵ the PrP^C structure has been solved by solution-state nuclear magnetic resonance (NMR) and crystallographic methods. PrP^C consists of a highly flexible N-terminal segment (residues 23–124) and a folded C-terminus domain (residues 125–231).^{15,16} The C-terminus domain contains three α -helices, spanning residues 144–154 (α 1), 173–194 (α 2), and 200–228 (α 3), and two short antiparallel β -strands comprising residues 128–131 (β 1) and 161–164 (β 2). The PrP expressed by mammalian species exhibits a similar fold, with the local sequence and structure variations most prominently localized at the interface of the β 2– α 2 loop and in the C-terminus part of the α 3 helix.¹⁷

Received: September 1, 2019

Accepted: November 6, 2019

Published: November 15, 2019

of NMR spectroscopy. A comparison to previously determined PrP structures from the white-tailed deer and Rocky Mountain elk^{36,37} provides insights that may contribute to our understanding of how the single polymorphism Q226E between deer and elk can alter the structure and help to explain the substantial differences in biochemical properties, pathogenesis, and formation of different strains of CWD prions among cervids.³⁸ We hypothesized that the presence of polymorphism Q226E, as the most critical for CWD among the six identified differences in amino acid sequences, could influence the long-range intramolecular interactions including the packing of the $\beta 2$ - $\alpha 2$ loop and the C-terminus of the $\alpha 3$ helix. This solvent-accessible epitope has been studied greatly in view of its role in prion conversion.^{39,40} Additionally, the changes from the neutral to negatively charged side chain at position 226 will influence the electrostatic surface potential in this region, which is of great relevance for the intermolecular interactions between PrP^C and PrP^{Sc} among cervids.

RESULTS AND DISCUSSION

Amino Acid Alignment and mdPrP Construct. The amino acid sequences of PrPs from various cervid subspecies related to CWD are highly evolutionary-conserved. The alignment of amino acid sequences of mdPrP, white-tailed deer (wtdPrP), elk (ePrP), red deer PrP (reddPrP), American moose PrP (amPrP), Eurasian moose PrP (emPrP), and reindeer PrP (rdPrP) showed differences in the amino acid residues at positions 109, 123, 138, 176, 209, and 226 (Figure 1; numbering is based on the amino acid sequence of the mdPrP construct used herein for structure determination). A simple perusal of the differences shows that the three of them are positioned within the well-defined secondary structural elements. Truncated recombinant mdPrP from residues 94 to 233 with serine at position 138 and glutamine at position 226 was used for structural characterization and comparison with previously resolved wtdPrP and ePrP structures.

Resonance Assignment and Structure Calculation. The ¹⁵N-heteronuclear single quantum coherence (HSQC) spectrum of ¹³C, ¹⁵N doubly labeled mdPrP presents a favorable dispersion of cross-peaks, indicating a high potential for in-depth structural determination (Figure 2). Standard two-dimensional and 3D NMR experiments were used for the assignment of backbone and side-chain resonances of mdPrP. In short, the sequence-specific assignment of the backbone ¹H, ¹⁵N, ¹³C _{α} , ¹³C _{β} , and ¹³CO resonances for mdPrP was obtained using the ¹⁵N-HSQC spectrum and triple-resonance HNCO, HN(CO)CA, HNCA, CBCA(CO)NH, and HNCACB experiments.⁴¹ The ¹H and ¹³C resonances of aliphatic and aromatic side chains were assigned using ¹³C-HSQC in combination with HAHB(CO)NH, CC(CO)NH, (H)CCH- total correlation spectroscopy (TOCSY), and ¹³C-edited nuclear Overhauser enhancement spectroscopy (NOESY)-HSQC experiments.⁴² NOE contacts were determined in 3D ¹⁵N and ¹³C-edited NOESY-HSQC experiments. The overall completeness of chemical shift assignment was 99.1%. Noteworthy, the side-chain resonances including CH _{ϵ} of His⁹⁹, His¹¹⁴, and Tyr¹⁵² and CH _{ζ} of Phe¹⁷⁸ and Phe²⁰¹ could not be unambiguously assigned; however, this agrees very well with the final structure and properties of the studied protein. We have considered the use of residual dipolar couplings for structure improvement, especially interhelical orientations. However, the use of aligning media was showed to induce sample precipitation of PrPs.

The high-resolution structure of mdPrP was calculated using 545 intraresidual, 618 sequential, 482 medium-range, and 559 long-range distance restraints complemented with 168 backbone torsion angle restraints (Table 1). The calculated

Table 1. NMR Restraints and Structural Statistics for an Ensemble of 20 Lowest Energy Structures of mdPrP

NOE upper distance limits ^a	
total	2204
intraresidue ($ i - j = 0$)	545
sequential ($ i - j = 1$)	618
medium-range ($1 < i - j < 5$)	482
long-range ($ i - j \geq 5$)	559
torsion angle restraints ^a	
backbone (φ/ψ)	168
rmsd to the mean coordinates (Å)	
ordered backbone atoms (123–231)	0.42 ± 0.08
ordered heavy atoms (123–231)	0.78 ± 0.09
Ramachandran plot (123–231) ^b	
residues in most favored regions (%)	95.0
residues in additional allowed regions (%)	5.0
structure Z scores ^b	
first generation packing quality	0.763 ± 0.513
second generation packing quality	5.102 ± 1.464
Ramachandran plot appearance	−0.453 ± 0.282
chi-1/chi-2 rotamer normality	−3.717 ± 0.483
backbone conformation	−0.541 ± 0.234
rms Z scores ^b	
bond lengths	1.143 ± 0.003
bond angles	0.465 ± 0.011
omega angle restraints	0.481 ± 0.032
side-chain planarity	0.358 ± 0.029
improper dihedral distribution	0.571 ± 0.017
inside/outside distribution	1.030 ± 0.011

^aNone of the 20 structures exhibits distance violations over 0.2 Å and torsion angle violation over 5°. ^bensemble of structures was analyzed by PROCHECK-NMR⁴³ and WhatIF programs incorporated in ICING structure evaluation package⁴⁴ and PSVS.⁴⁵

structure of mdPrP (PDB ID: 6FNV) is composed of two distinct domains. The highly disordered N-terminal domain consists of residues from Gly⁹⁴ to Gly¹²², whereas the well-defined C-terminus domain is composed of residues from Ala¹²³ to Ala²³³ and exhibits a backbone root-mean-square deviation (rmsd) of 0.42 Å (Figure 3A and Table 1).

The C-terminus domain of mdPrP is characterized by a compact set of three α -helices and a short antiparallel β -sheet. The $\alpha 1$ helix is composed of residues from Asp¹⁴⁷ to Asn¹⁵⁶ and is followed by the 3_{10} -helix turn from Met¹⁵⁷ to Arg¹⁵⁹. The geometry of $\alpha 1$ helix is classified as kinked according to the HELANAL web server.^{46,47} The $\alpha 2$ and $\alpha 3$ helices are longer than the $\alpha 1$ helix and are composed of residues from Gln¹⁷⁵ to Lys¹⁹⁷ and from Glu²⁰³ to Gln²³⁰, respectively. The geometries of $\alpha 2$ and $\alpha 3$ helices are linear and of curved type, respectively. The helices $\alpha 2$ and $\alpha 3$ form a twisted V-shaped skeleton that serves as a platform for anchoring the $\alpha 1$ helix and β -sheet. The antiparallel β -sheet is formed at the beginning of the C-terminus domain and consists of two β strands, $\beta 1$ and $\beta 2$, that are composed of residues from Met¹³² to Leu¹³³ and from Tyr¹⁶⁵ to Tyr¹⁶⁶, respectively. The structure of mdPrP is

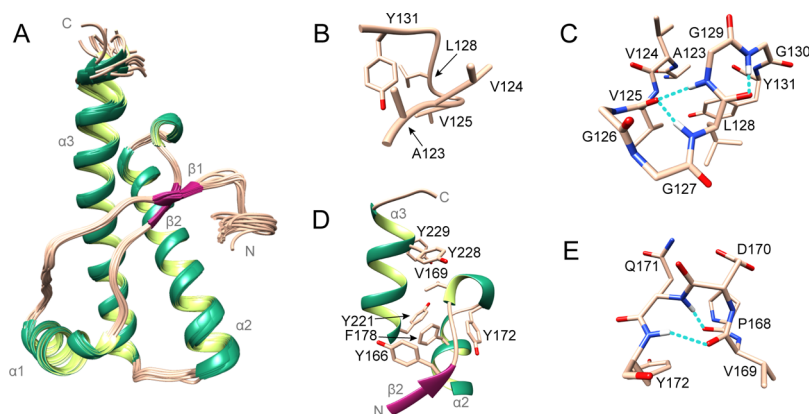


Figure 3. Structure of mdPrP. (A) Ensemble of 20 lowest energy structures of mdPrP (residues from Ala¹²³ to Ala²³³). α -Helices and 3_{10} -helix are colored green, β -sheets are colored magenta, and loops are colored champagne pink. (B) Well-defined region between residues Ala¹²³ and Tyr¹³¹. (C) Residues from Ala¹²³ to Tyr¹³¹ involved in the formation of α -helical turn (Val¹²⁵–Leu¹²⁸) and γ -turn (Leu¹²⁸–Gly¹³⁰). (D) Hydrophobic pocket in the proximity of the $\beta 2$ – $\alpha 2$ loop and the C-terminus of the $\alpha 3$ helix. (E) 3_{10} -Helix from residues Pro¹⁶⁸ to Tyr¹⁷² inside the $\beta 2$ – $\alpha 2$ loop. Residues are presented as sticks in champagne pink and the hydrogen bonds in panels (C,E) are shown as dashed lines in cyan.

stabilized by a disulfide bond between Cys¹⁸² and Cys²¹⁷ that is located in the middle of $\alpha 2$ and $\alpha 3$ helices.

Unique Structural Features of the mdPrP Protein. We observed the structuring of the region at the beginning of the C-terminus domain of mdPrP. This region consists of nine residues from Ala¹²³ to Tyr¹³¹ and adopts a well-defined structure with the backbone rmsd of 0.22 Å (Figure 3B). It is characterized by an α -helical turn and a γ -turn that are stabilized by three hydrogen bonds (Figure 3C). The carbonyl group of Val¹²⁵ is involved in a bifurcated hydrogen bond with the amide protons of Leu¹²⁸ and Gly¹²⁹ in the α -helical turn. In addition, a hydrogen bond is formed between the carbonyl group of Leu¹²⁸ and the amide proton of Gly¹³⁰ in the γ -turn. An hydrophobic pocket in this region is formed by Val¹²⁵, Leu¹²⁸, and Tyr¹³¹ (Figure 3B,C).

Additionally, the $\beta 2$ – $\alpha 2$ loop of the mdPrP structure is well defined with one turn of 3_{10} -helix from the residues Val¹⁶⁹ to Gln¹⁷¹ (Figure 3D) held together by the Gln¹⁷¹H^N–Pro¹⁶⁸O and Tyr¹⁷²H^N–Val¹⁶⁹O hydrogen bonds (Figure 3E). The $\beta 2$ – $\alpha 2$ loop is further stabilized by hydrophobic and aromatic interactions with the nearby amino acid residues at the C-terminus of the $\alpha 3$ helix. The hydrophobic pocket defined by the $\beta 2$ – $\alpha 2$ loop and the C-terminus of the $\alpha 3$ helix is composed of residues Tyr¹⁶⁶, Val¹⁶⁹, Tyr¹⁷², Phe¹⁷⁸, Tyr²²¹, and Tyr²²⁸ (Figure 3D).

The above structuring of the region before the well-defined C-terminus domain and the $\beta 2$ – $\alpha 2$ loop is supported further with the study of backbone dynamics. We analyzed 118 resolved amide resonances of mdPrP on a fast (picoseconds to nanoseconds) timescale with the use of ¹⁵N relaxation time measurements at two magnetic fields (14.1 and 18.8 T). The resulting ¹⁵N longitudinal (R_1), transverse (R_2), and rotating frame ($R_{1\rho}$) relaxation rates combined with ¹H–¹⁵N heteronuclear NOE (hNOE) conform to the flexible N-terminal tail and a well-structured C-terminus domain of the mdPrP structure (Figure 4).

Furthermore, ¹⁵N relaxation data indicate structuring for residues from Ala¹²³ to Tyr¹³¹ at the beginning of the C-terminus domain and for the $\beta 2$ – $\alpha 2$ loop. On the other hand, ¹⁵N relaxation data show an increased mobility for residues from Lys¹⁹⁷ to Phe²⁰¹ that connect $\alpha 2$ and $\alpha 3$ helices and for residues from Tyr²²⁹ to Ala²³³ at the C-terminus of the mdPrP structure. However, the relative lower values of R_2 and $R_{1\rho}$

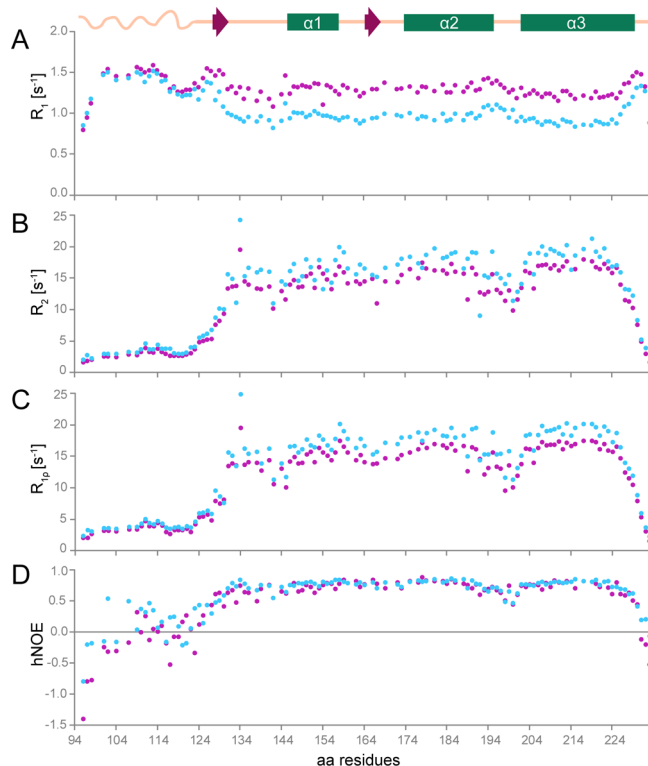


Figure 4. ¹⁵N amide backbone relaxation rates and hNOE of mdPrP. (A) ¹⁵N longitudinal ($R_1 = 1/T_1$), (B) transverse ($R_2 = 1/T_2$), (C) spin–lattice relaxation rates in the rotation frame ($R_{1\rho} = 1/T_{1\rho}$), and (D) hNOE at 298 K at a magnetic field of 14.1 (magenta) and 18.8 T (blue). A schematic presentation of the secondary structure elements of mdPrP is at the top of the figure. For clarity, error bars are not shown here as they are within the size of the data points in the above graphics but are presented in the Supporting Information in Figure S1.

relaxation rates for residues around Ile¹⁴² and Gln¹⁸⁹ are not indicative of a well-defined secondary structure and suggest more complex dynamics coupled to their intricate tertiary interaction. Few amino acid residues could not be analyzed because of the cross-peak overlap (for details, see Methods).

Comparison of Structures of mdPrP and Other Cervids. Cervid prion proteins exhibit a well-conserved

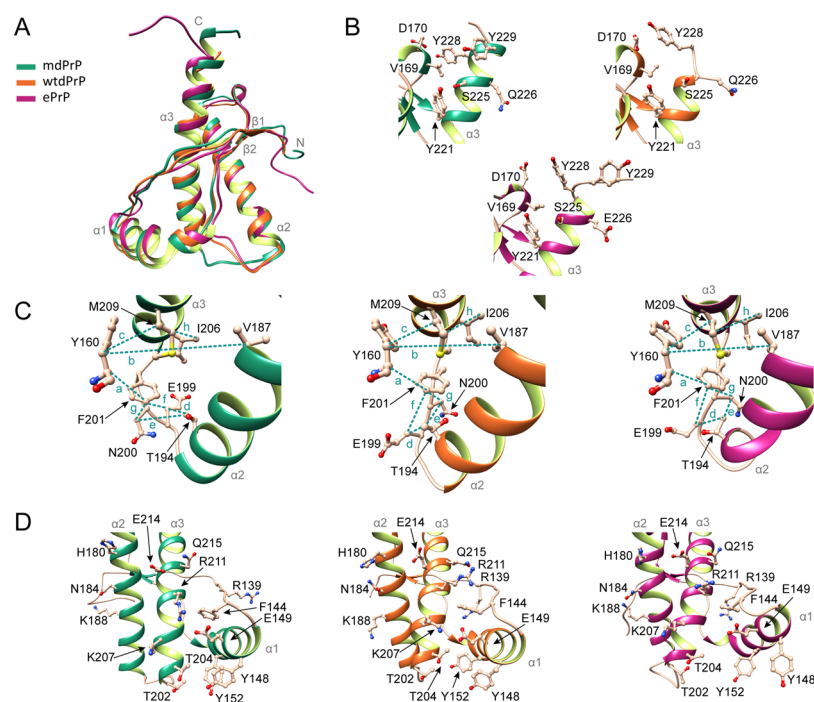


Figure 5. Comparison of mdPrP, wtdPrP, and ePrP structures. (A) Superposition of well-defined C-terminus domains from amino acids Ala¹²³–Ala²³³ of mdPrP (green), wtdPrP (orange), and ePrP (magenta). The selected residues are presented as ball-and-stick and colored in champagne pink with marked heteroatoms. (B) Structural diversity at the end of the $\alpha 3$ helix and the $\beta 2$ – $\alpha 2$ loop. (C) Spatial orientation of residues in the proximity of the $\alpha 2$ – $\alpha 3$ loop with marked distances. Selected distances among residues are indicated with dashed lines and small letters (see Table 2 for distance information). (D) Structural differences in orientations at the $\alpha 1$ helix with respect to the $\alpha 2$ – $\alpha 3$ V-shaped skeleton.

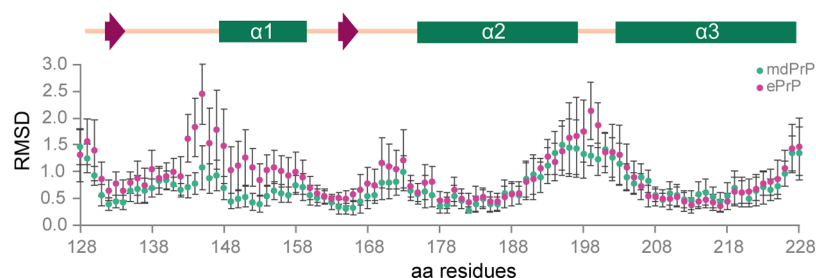


Figure 6. Local rmsd values for backbone atoms per residue (from 128 to 228) of mdPrP (green) and ePrP (magenta) with respect to the wtdPrP structure that was determined by X-ray. Standard deviations are reported for the ensemble of 20 lowest energy structures of mdPrP and ePrP.

amino acid sequence, which may suggest similarity of their 3D structures. We compared our mdPrP structure with the structures of previously determined PrPs from white-tailed deer and Rocky mountain elk and observed several differences. For easier comparison of cervids' PrP structures, we unified the residue numbering based on the mdPrP amino acid sequence. Here, we have to mention that the wtdPrP structure was determined in complex with an antibody fragment POM1 at pH 6.8; however, the PDB entry for wtdPrP includes residues from 128 to 228 (PDB ID: 4YXH).³⁶ The ePrP structure consists of residues from 124 to 234 (PDB ID: 1XYW) and was determined at pH 4.5.³⁷ We used pH of 5.5 for structure determination because the lower pH prevents aggregation and enables longevity of the prion protein samples that is necessary for structure determination by NMR spectroscopy. Additionally, it has been suggested that misfolding of PrPs in prion disease occurs in endosomes that exhibit a low pH (pH \approx 5).⁴⁸ In general, the fold of mdPrP is grossly similar to wtdPrP and ePrP structures (Figure 5A), even though the structures were determined under different sample conditions.

We compared the chemical shifts (δ) of amide proton (H^N), $C\alpha$, and $C\beta$ atoms of amino acids from 124 to 233 between the mdPrP and ePrP structures determined by NMR spectroscopy (Figure S2). The chemical shifts of H^N , $C\alpha$, and $C\beta$ atoms of mdPrP and ePrP showed good agreement along the sequence. Slight, if not negligible, differences have been observed for $\delta(H^N)$ and $\delta(C\alpha)$ for the amino acid residues in the $\alpha 2$ – $\alpha 3$ loop, which could indicate different long-range interactions among amino acids in this region. The calculated rmsd for the protein backbone of the three compared structures (residues 128–228) is 1.2 Å. The local backbone rmsd values per residue are in good agreement with the observed differences among the examined structures (Table S1, Figures 5 and 6). The main differences in backbone rmsd values between the mdPrP and ePrP structures have been detected at the N-terminal of the $\alpha 1$ helix and at the $\alpha 2$ – $\alpha 3$ loop (Figure 6).

However, despite a very high level of numerical similarity, structural differences are observed at the beginning of the C-terminus domains, $\beta 2$ – $\alpha 2$ loops and their interactions with $\alpha 3$

helices, at the beginning of $\alpha 1$ helices and their interactions with $\alpha 2$ and $\alpha 3$ helices, and $\alpha 2$ – $\alpha 3$ loops (Figures 5 and S3).

Residues from Val¹²⁴ to Gly¹³⁰ in ePrP exhibit an extended backbone conformation. Similarly, the residues from Leu¹²⁸ to Gly¹³⁰ in the wtdPrP structure have no observed structuring. Both regions of ePrP and wtdPrP structures exhibit no hydrogen bonds in contrast to mdPrP, where we observed three hydrogen bonds (Figures 3C, 5A and S3). No hydrophobic pocket was observed in this region of ePrP or wtdPrP structures, whereas mdPrP exhibits a well-defined hydrophobic pocket composed by the residues Val¹²⁵, Leu¹²⁸, Tyr¹³¹, and Ile¹⁸⁵. The backbone structures of the three proteins exhibit similar conformations after the residue Gly¹³⁰. Interestingly, within the examined structures, Tyr¹³¹ exhibits a diverse side-chain orientation and distinct stacking with Tyr¹⁶⁶ and Ile¹⁸⁵. The relative position of Tyr¹³¹ side chain and its interactions with the residues in proximity might have an impact on the formation of the α -helical turn and γ -turn in mdPrP in contrast to wtdPrP and ePrP. Solvent accessibility analysis with the GETAREA program^{49,50} showed that the Tyr¹³¹ residue is protected from exchange with solvents in all three structures (Figure S4). However, the distance between Tyr¹³¹ and Ile¹⁸⁵ in the $\alpha 2$ helix is 2 times longer in mdPrP and ePrP structures in comparison to the wtdPrP structure (Table S2). In contrast, the distance between Leu¹²⁸ and Ile¹⁸⁵ is shorter in the mdPrP structure with respect to the distances in ePrP and wtdPrP structures (Table S2). These observations indicate differences in interactions between the $\beta 1$ – $\alpha 1$ – $\beta 2$ and $\alpha 2$ – $\alpha 3$ subdomains of the compared structures. It was previously proposed that different side-chain orientations of Tyr¹³¹ play an important role in the interactions between these subdomains and furthermore could also affect the flexibility of the $\beta 2$ – $\alpha 2$ loop region.^{36,55} In this way, the region from the residues Ala¹²³ to Tyr¹³¹ could additionally stabilize the mdPrP structure through its interactions with the antiparallel β -sheet and $\alpha 2$ helix and in this way prevent PrP^C-to-PrP^{Sc} conversion.

The $\beta 2$ – $\alpha 2$ loop of mdPrP comprising residues 168–178 is well-defined, composed of 3_{10} -helix, and stabilized with aromatic and hydrophobic interactions with the nearby residues. The backbone orientations of $\beta 2$ – $\alpha 2$ loops of the three examined structures are similar, whereas small differences are notable in the side-chain orientations of Val¹⁶⁹ and Asp¹⁷⁰ (Figure 5B). Moreover, different orientations of glutamine and asparagine side chains in the $\beta 2$ – $\alpha 2$ loops (residues Gln¹⁷¹, Asn¹⁷³, Asn¹⁷⁴, and Asn¹⁷⁶) are observed and might be related to the long-range interactions and orientations of the aromatic moiety of Tyr¹³¹ in the three compared structures (Figure S3). The structural features of $\beta 2$ – $\alpha 2$ loop have been extensively discussed in the literature.^{22,56–60} The presence of Asn/Gln residues in the $\beta 2$ – $\alpha 2$ loop can be a strong determinant for prion conversion that overrides the differences in the sequence and has influence on the appearance of prions according to the zipper model between the cervid and human PrP.²² Moreover, insertion of additional Gln residues into the $\beta 2$ – $\alpha 2$ loop of mouse PrP promotes prion protein conversion,^{61–63} whereas several substitutions (at positions 169, 171, 173, and 177; residues numbering based on the mdPrP sequence) in the $\beta 2$ – $\alpha 2$ loop of PrP^C are believed to prevent the spontaneous prion formation by influencing the structural stability of the $\beta 2$ – $\alpha 2$ loop.^{56–59,64}

Additionally, the structures and interactions of side chains in the $\beta 2$ – $\alpha 2$ loops are influenced by the orientations of side chains in the C-terminus of the $\alpha 3$ helix including the residue

at position 226. The $\alpha 3$ helix of wtdPrP is shorter and ends with Ser²²⁵, possibly because of the shorter amino acid sequence³⁶ with respect to the mdPrP structure. The C-terminus of ePrP protein is unstructured after Tyr²²⁸ (Figure 5B). Tyr²²⁸ and Tyr²²⁹ have different side-chain orientations in mdPrP in comparison to the ePrP structure, as a result of their distinct relative orientation, that lead to hydrophobic interactions with the residues Val¹⁶⁹, Asp¹⁷⁰, and Ser²²⁵ and additionally stabilize the end of the C-terminus part in mdPrP (Figure 5B and Table S2). Tyr²²⁸ of the wtdPrP structure is involved in stacking interactions with Asp¹⁷⁰ in the $\beta 2$ – $\alpha 2$ loop. However, the interactions between the residues at the end of the $\alpha 3$ helix and Gln²²⁶ are not observed in wtdPrP, resulting in higher solvent accessibility of Ser²²⁵ and Gln²²⁶ in comparison to mdPrP and ePrP (Figures 5B and S3). Importantly, beside the polymorphism Q226E, mule deer exhibits serine-to-asparagine polymorphism at position 138, which is processed as a pseudogene,^{69,70} and serine-to-phenylalanine polymorphism at codon 225.³⁰ Allele Phe²²⁵ in mule deer could contribute to CWD resistance in view of the reported prolonged incubation period with respect to the Ser²²⁵ mule deer homozygote.³⁰ Interestingly, it has been shown that polymorphisms at residues 225 and 226 affect the interactions between the $\beta 2$ – $\alpha 2$ loop and $\alpha 3$ helix and therefore prion propagation within deer and elk.^{40,71} Our results showed that Ser²²⁵ is protected from solvents as it is involved in the interaction with Tyr²²⁸ in mdPrP. Additionally, Tyr²²⁸ in mdPrP is protected from solvents by the stacking interaction with Val¹⁶⁹. These data contribute to the understanding at the molecular level and are in agreement with the structural and molecular dynamics studies of inter- and intraspecies PrP transmission related to cervids that pointed out a critical role of residues 225 and 226 in PrP^C-to-PrP^{Sc} conversion and strain propagation.⁴⁰

In the three structures, $\alpha 2$ and $\alpha 3$ helices form a V-shaped skeleton that slightly differs in the spatial orientation of the helices. The interhelical angle between the $\alpha 2$ and $\alpha 3$ helices of mdPrP is 44.5°, whereas its value in wtdPrP and ePrP is 49.8 and 52.2°, respectively. The hydrophobic and aromatic residues of $\alpha 2$ and $\alpha 3$ helices have preserved architectures that are stabilized by a disulfide bond in the three structures. However, significant differences are observed for the side-chain orientations of His¹⁹⁰ and Thr¹⁹⁴ in the $\alpha 2$ helix and Ile²⁰⁶, Met²⁰⁹, and Glu²¹⁰ in the $\alpha 3$ helix (Figures 5C and S1). These residues are spatially close to the loop that connects $\alpha 2$ and $\alpha 3$ helices. Surprisingly, the $\alpha 2$ – $\alpha 3$ loop of mdPrP exhibits a unique backbone conformation with different orientations of the side chains of Glu¹⁹⁹, Asn²⁰⁰, and Phe²⁰¹ with respect to wtdPrP and ePrP. However, the hydrophobic interactions of Phe²⁰¹ and Tyr¹⁶⁰ are preserved in the three structures. Major differences are observed for distances Tyr¹⁶⁰C _{α} –Val²⁰¹C _{β} and Glu¹⁹⁹C _{β} –Phe²⁰¹C _{ζ} that are up to 2 Å longer in mdPrP with respect to wtdPrP and ePrP (Table 2). The opposite is observed for distances Thr¹⁹⁴C _{$\gamma 2$} –Asn²⁰⁰C _{β} , Asn²⁰⁰C _{β} –Phe²⁰¹C _{ζ} , and Ile²⁰⁶C _{$\gamma 2$} –Met²⁰⁹C _{γ} that are shorter in mdPrP with respect to the other two cervid structures (Figure 5C and Table 2). The residue Glu¹⁹⁹ is more exposed to the solvents, whereas residue Asn²⁰⁰ is less solvent-exposed in mdPrP in comparison to wtdPrP and ePrP (Figure 7). Different side-chain orientations in the $\alpha 2$ – $\alpha 3$ loop could influence the interactions of residues in helices that are spatially close to this region. In early events of oligomerization, it is believed that the $\alpha 1$ helix moves away from the $\alpha 2$ – $\alpha 3$ V-shaped skeleton. This

Table 2. Distances between C Atoms of Selected Amino Acid Residues in Proximity of the $\alpha 2$ – $\alpha 3$ Loop in mdPrP, wtdPrP, and ePrP Structures^a

mark ^b	distance	mdPrP (Å)	wtdPrP (Å)	ePrP (Å)
A	Tyr ¹⁶⁰ C _{α} –Phe ²⁰¹ C _{ζ}	6.5 ± 0.3	5.3	5.5 ± 0.4
B	Tyr ¹⁶⁰ C _{β} –Val ¹⁸⁷ C _{β}	11.5 ± 0.4	9.1	8.9 ± 0.3
C	Tyr ¹⁶⁰ C _{β} –Met ²⁰⁹ C _{β}	5.2 ± 0.1	4.7	5.1 ± 0.3
D	Thr ¹⁹⁴ C _{$\gamma 2$} –Glu ¹⁹⁹ C _{β}	4.8 ± 0.4	5.7	4.2 ± 0.6
E	Thr ¹⁹⁴ C _{$\gamma 2$} –Asn ²⁰⁰ C _{β}	5.7 ± 0.5	8.3	6.4 ± 1.3
F	Glu ¹⁹⁹ C _{β} –Phe ²⁰¹ C _{ζ}	7.3 ± 0.5	6.8	6.5 ± 0.7
G	Asn ²⁰⁰ C _{β} –Phe ²⁰¹ C _{ζ}	4.0 ± 0.2	7.5	7.5 ± 0.4
H	Ile ²⁰⁶ C _{$\gamma 2$} –Met ²⁰⁹ C _{γ}	4.8 ± 0.1	6.5	6.8 ± 0.2

^aReported distances are average values obtained from the coordinates of the structural ensemble for mdPrP (PDB id 6FNV) and ePrP (PDB id 1XYW) that were determined by NMR and for wtdPrP (PDB id 4YXH) determined by X-ray crystallography. Standard deviations are reported for the ensemble of 20 lowest energy structures for mdPrP and ePrP. ^bLetters specify the position of distances in Figure 5C.

is responsible for the increased local structural dynamics that is reflected in greater exposure of the amide hydrogen atoms in the $\alpha 1$ helix of mouse PrP.^{65–68} Importantly, the stabilization of interactions or covalent linkage by a disulfide bond between the subdomains $\beta 1$ – $\alpha 1$ – $\beta 2$ and $\alpha 2$ – $\alpha 3$ is supposed to prevent the oligomerization.⁶⁵

Structure variations were also observed in the orientations of the three helices and at the end of the $\alpha 1$ helix and its interactions with the $\alpha 2$ – $\alpha 3$ loop. The aromatic interactions between Tyr¹⁴⁸ and Tyr¹⁵² differ among the three structures (Figure 5D). Furthermore, 2 times shorter distances of Tyr¹⁴⁸ with Thr²⁰² and Thr²⁰⁴ are observed in mdPrP and ePrP structures compared to wtdPrP (Table S2). A similar trend in distances was observed between Tyr¹⁵² and Thr²⁰². In contrast, the distances between Tyr¹⁵² and Thr²⁰⁴ are similar for all the three structures. Thr²⁰² and Thr²⁰⁴ are more solvent-exposed in the ePrP structure with respect to mdPrP and wtdPrP structures (Figure 7). We observed a closer anchoring of the $\alpha 1$ helix to $\alpha 2$ and $\alpha 3$ helices in the mdPrP structure with respect to ePrP and wtdPrP.

Effect of Polymorphism Q226E on Electrostatic Surface Potential. MdPrP, wtdPrP, and ePrP are known for their polymorphisms at positions 138 and 226. S138N and Q226E polymorphisms have a major impact on the electrostatic surface potential of the examined structures (Figure 8).

Our results show that variations in the electrostatic surface potential among the three proteins are mostly clustered at the $\beta 1$ – $\alpha 1$ loop, at the beginning of the $\alpha 2$ helix, at the V-shaped skeleton where the antiparallel β sheet is in proximity to the $\alpha 2$

and $\alpha 3$ helices, and at the C-terminus of the $\alpha 3$ helix (Figure 8).

In contrast to the wtdPrP and ePrP structures, a large contiguous area of positive electrostatic potential is observed on the surface of the mdPrP structure. The region around residue 138 is positively charged in mdPrP, whereas the corresponding region in wtdPrP and ePrP proteins is neutral. Additional variations of positive charge in the mdPrP and wtdPrP structures to a predominantly neutral state in the ePrP structure are observed in the middle of $\alpha 2$ and $\alpha 3$ helices. Polymorphism Q226E is reflected in the charge of preferentially positive surface areas in the $\beta 2$ – $\alpha 2$ loop and the C-terminus of the $\alpha 3$ -helix in mdPrP and wtdPrP in comparison to the negative electrostatic potential in ePrP. However, the C-terminus of wtdPrP is negatively charged to mdPrP and ePrP. Residues 225 and 226 are located in a distal region of the $\alpha 3$ helix that participates in interactions with the $\beta 2$ – $\alpha 2$ loop to form a solvent-accessible contiguous epitope.⁷² Our data suggest that different distributions of electrostatic potential between mdPrP and ePrP proteins may facilitate intramolecular interactions between two allelic variants in deer subspecies in case of S225F and Q226E polymorphisms and influence the early stages of prion conversion and neuropathology of CWD among cervids.

CONCLUSIONS

The spread of CWD in North America and the most recent cases of CWD-infected cervid subspecies in Europe have raised concerns for public health and perceived risks for possible CWD transmission to humans through the consumption of CWD-infected venison.^{8,51–53} The possible spontaneous spread of the disease among cervid subspecies in Eurasia represents a global threat.⁵⁴ Structural studies on mdPrP at the molecular level are important for understanding the still unknown reasons for the appearance of the detected and confirmed cases of CWD in captive mule deer³ and the progressive spread and identification of the disease in other cervids.

Previous findings suggest that the primary structural differences at residue 226 identify biologically distinct prion strains on the basis of different disease progressions in deer and elk³³ and have a role in dictating the selection of different CWD prion strains in gene-targeted mice.³⁵ These findings suggest that the observed differences are related to an altered structure of PrP^C caused by the Q226E polymorphism, highlighting the importance of amino acid sequence variations affecting the local changes of 3D structures, whereas the globular fold remains similar. A detailed comparative structural

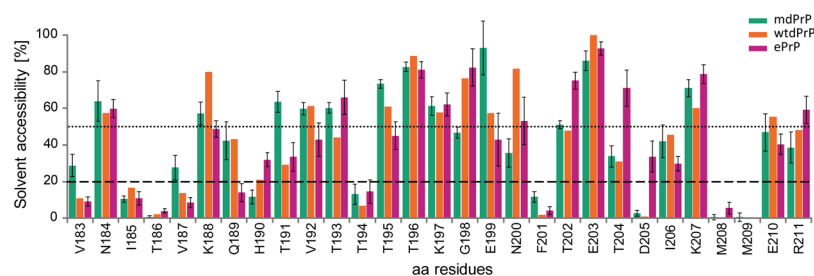


Figure 7. Solvent accessibility of selected residues that belong to the $\alpha 2$ and $\alpha 3$ helices. Hatched and dotted lines at 20 and 50% indicate the limits of amino acid residue accessibility to solvents (>50%) or burial in solvent-inaccessible regions (<20%). Standard deviations are reported for the ensemble of 20 lowest energy structures of mdPrP and ePrP that have been determined by NMR.

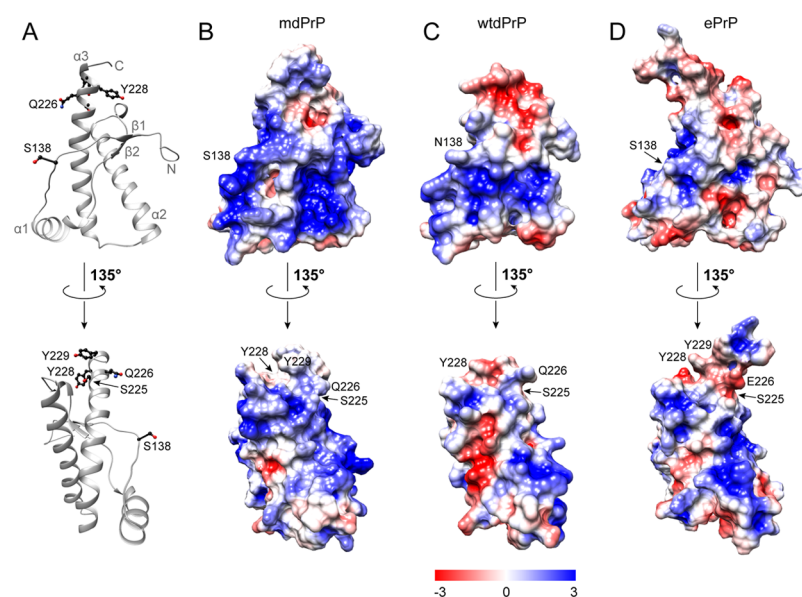


Figure 8. Electrostatic surface potential of the three cervid PrPs. (A) Ribbon presentation of the mdPrP backbone orientation used in panels (B–D). Residues Ser¹³⁸, Ser²²⁵, Gln²²⁶, Tyr²²⁸, and Tyr²²⁹ are presented as ball-and-stick and colored black. Electrostatic surface potentials of (B) mdPrP, (C) wtdPrP, and (D) ePrP. Regions of positive and negative charges are depicted from blue to red according to the presented charge legend. Orientation of structures is preserved in all panels. The lower set of structures is rotated by 135°.

analysis of the examined PrP of cervids could provide insights into pathogenesis suggesting that the structures of deer and elk prion proteins may determine prion strain mutation in these cervids.

Our comparative analysis uncovered the structural determinants of mdPrP that are manifested in diverse structural rearrangements and distinct electrostatic surface potentials with respect to the wtdPrP and ePrP structures. The region at the beginning of the C-terminus domain could protect the β -sheet from solvents, force the closer packing of $\beta 1$ – $\alpha 1$ – $\beta 2$ to $\alpha 2$ – $\alpha 3$ subdomains and raise the structural stability of mdPrP. These structural features could have a major effect on the prion conversion. In our previous studies, we have found that amino acid substitution at position 226 has dramatic effects on CWD prion replication, pathogenesis, and biochemical properties.⁷³ Tg(DeerPrP) has a longer incubation time compared with Tg(ElkPrP) mice after inoculation with CWD prions. On the other hand, Tg(DeerPrP) mice were susceptible to SSBP/1,⁷⁴ whereas Tg(ElkPrP) mice were completely resistant.⁷¹ In addition, Q226 CWD prions display more resistance to guanidine denaturation than the E226 CWD prions.³⁵ Our current findings suggest that the long-range interactions in the mdPrP protein might stabilize the overall structure, thus impacting the PrP^C-to-PrP^{Sc} conversion. The distribution of electrostatic surface potential on the mdPrP protein may lead to different intermolecular interactions between PrP^C and PrP^{Sc} and in this way may represent a step toward understanding the underlining mechanism of CWD prion transmission.

METHODS

Plasmid Construction for NMR Sample Preparation.

The recombinant dePrP (94–233) was obtained using the QuikChange kit (Stratagene) utilizing primers 5'-CAGAGA-GAATCCCAGGCTTATTACCAAAGA-3' and 5'-TCTTTGGTAATAAGCCTGGGATTCTCTCTG-3' and ePrP(94–234) as templates. The DNA product was then

inserted into pProExHTa (Invitrogen), containing the cleavage site between the His₆ tag and the protein fragment. The cloned DNA sequences were verified by sequencing.

Prion Protein Expression and Purification. A freshly transformed overnight culture of *E. coli* BL21 (DE3) cells (Stratagene) was added at 37 °C to 2 L of the minimal medium plus ampicillin (100 mg/mL). For isotope labeling, 4 g/L [¹³C₆] glucose and 1 g/L [¹⁵N] ammonium chloride were added. At 0.8 OD₆₀₀, expression was induced with isopropyl β -D-galactopyranoside to a final concentration of 0.8 mM. Cells were grown in a Biostat B plus 2 L vessel (Sartorius) and harvested 18 h after inoculation. The bacterial paste was resuspended in 25 mM Tris-HCl, 0.8% Triton X-100, and 1 mM phenylmethylsulfonyl fluoride, pH 8.0, and lysed by a Panda homogenizer. A crude extract was loaded onto a 5 mL HisTrap column (GE Healthcare) equilibrated in a binding buffer [2 M GndHCl, 500 mM NaCl, 20 mM Tris-HCl, and 20 mM imidazole (pH 8.0)] and eluted with 500 mM imidazole. The purified protein was lyophilized and dissolved in 8 M GndHCl. The protein was diluted to a final concentration of 0.5 mg/mL in a tobacco etch virus (TEV) reaction buffer (50 mM Tris base, 1 mM ethylenediaminetetraacetic acid, and 5 mM dithiothreitol), and TEV protease was added to the final concentration of 75 μ g/mL. The reaction was incubated at 22 °C overnight. The cleaved sample was loaded onto a 5 mL HisTrap column (GE Healthcare) equilibrated with a binding buffer [500 mM NaCl and 20 mM Tris-HCl (pH 8.0)], and the flow-through containing only the cleaved protein was collected. The purified protein was lyophilized and redissolved in 8 M GndHCl. Refolding was performed by dialysis against a refolding buffer [20 mM sodium acetate and 0.005% Na₂S₂O₃ (pH 5.5)] using a Spectra/Por membrane (molecular weight, 3000). The purified protein was analyzed by sodium dodecyl sulfate polyacrylamide gel electrophoresis under reducing conditions, western blot, and electrospray mass spectrometry. The purification and expression of TEV protease were obtained as described earlier.⁷⁵

NMR Spectroscopy and Structure Calculation. All NMR experiments used for structure determination were performed on a ^{13}C , ^{15}N isotopically labeled mdPrP sample on a Varian VNMRs 800 MHz spectrometer equipped with a triple $^1\text{H}/^{13}\text{C}/^{15}\text{N}$ resonance cryogenic probe head operating at 25 K with inverse detection. The sample temperature was calibrated using the methanol- d_3 standard sample to ensure consistent sample temperature. The sample temperature for all experiments was 298 K. The sample contained 0.48 mM of mdPrP in a 20 mM sodium phosphate buffer, pH 5.5. NMR experiments for NH and HC detection were performed in 90%/10% $\text{H}_2\text{O}/\text{D}_2\text{O}$ and in a 100% deuterated buffer, respectively. The sequence-specific assignment of the backbone ^1H , ^{15}N , $^{13}\text{C}_\alpha$, $^{13}\text{C}_\beta$, and ^{13}C resonances for mdPrP was obtained using the ^{15}N -HSQC spectrum and triple-resonance NMR experiments HNC(O), HN(CO)CA, HNCA, CBCA-(CO)NH, and HNCACB.⁴¹ The ^1H and ^{13}C resonances of aliphatic and aromatic side chains were assigned using ^{13}C -HSQC in combination with HAHB(CO)NH, CC(CO)NH, (H)CCH-TOCSY, and ^{13}C -edited NOESY-HSQC experiments.⁴² NOE contacts were determined in 3D ^{15}N and ^{13}C -edited NOESY-HSQC experiments. Structure modeling of mdPrP was performed using the program CYANA 3.1.⁷⁶ Structure refinement using the explicit solvent model was performed by the YASARA program.⁷⁷ An ensemble of 20 lowest energy structures of mdPrP was validated by the web server software ICING⁴⁴ and PSVS.⁴⁵

Backbone amide relaxation measurements including ^{15}N longitudinal (R_1), transverse (R_2), rotating frame ($R_{1\rho}$) relaxation rates, and $\{^1\text{H}\}$ - ^{15}N heteronuclear NOE were obtained at two different magnetic fields (14.1 and 18.8 T) at 298 K.⁷⁸ Residues Gln⁹⁵, Thr⁹⁸, Ser¹⁰⁰, Asn¹⁰³, Ser¹⁰⁶, Met¹³⁷, His¹⁴³, Tyr¹⁶⁵, Asp¹⁷⁰, Gln¹⁷¹, Asn¹⁷⁴, Asn¹⁷⁶, His¹⁸⁰, Cys¹⁸², Val¹⁸⁷, Met²¹⁶, and Ile²¹⁸ could not be analyzed because of the cross-peak overlap.

All recorded spectra were processed with NMRPipe software⁷⁹ and analyzed with CARA⁸⁰ and SPARKY software.⁸¹ The prediction of backbone dihedral angles was made by the TALOS+ program.⁸² Alignment was prepared using ClustalO.⁸³ An analysis was performed by the web server GETAREA.^{49,50} The potentials were calculated at an experimental pH of 5.5 of mdPrP using PDB2PQR server,⁸⁴ APBS,⁸⁵ and PROPKA.^{86,87}

■ ASSOCIATED CONTENT

● Supporting Information

The Supporting Information is available free of charge on the ACS Publications website at DOI: 10.1021/acsomega.9b02824.

^{15}N amide backbone relaxation rates and hNOE of mdPrP; chemical shifts of H^{N} , C_α , and C_β atoms of mdPrP and ePrP structures; structural diversity of mdPrP, wtdPrP, and ePrP; and solvent accessibility of the selected amino acid residues of mdPrP, wtdPrP, and ePrP (PDF)

■ AUTHOR INFORMATION

Corresponding Authors

*E-mail: legname@sisia.it. Phone: +39 040 3787 715. Fax: +39 040 3787 702 (G.L.).

*E-mail: janez.plavec@ki.si. Phone: +386 47 60 353 (J.P.).

ORCID

Gabriele Giachin: 0000-0001-7550-0307

Janez Plavec: 0000-0003-1570-8602

Author Contributions

U.S. and G.S. contributed equally. The manuscript was written through contributions of all authors. All authors have given approval to the final version of the manuscript.

Funding

Funding was provided by the Slovenian NMR center through the Slovenian Research Agency grant no. P1-0242 and the CERIC-ERIC Consortium for access to experimental facilities. This work was also supported by a fellowship from the HEAd “Higher Education and Development” project (funded by the Friuli Venezia Giulia autonomous Region (Italy) through the Operational Program of the European Social Fund 2014/2020; grant no. FP1619889004) (to G.S.).

Notes

The authors declare no competing financial interest.

The atomic coordinates and structure factors of mdPrP (UniProtKB—P47852, PRIO_ODOHE) have been deposited in the Protein Data Bank (PDB ID: 6FNV) and Biological Magnetic Resonance Bank (BMRB ID: 34236).

■ ABBREVIATIONS

δ , chemical shift; amPrP, America moose prion protein; CWD, chronic wasting disease; ePrP, elk prion protein; emPrP, Eurasian moose prion protein; HSQC, heteronuclear single quantum coherence; hNOE, $\{^1\text{H}\}$ - ^{15}N heteronuclear nuclear Overhauser enhancement; mdPrP, mule deer prion protein; PrP, prion protein; PrP^C, cellular isoform of prion protein; PrP^{Sc}, prion-protease-resistant and infectious isoform; R_1 , longitudinal relaxation rate ($1/T_1$); R_2 , transverse relaxation rate ($1/T_2$); $R_{1\rho}$, relaxation rate in rotating frame ($1/T_{1\rho}$); reddPrP, red deer prion protein; rdPrP, reindeer prion protein; TOCSY, total correlation spectroscopy; TSE, transmissible spongiform encephalopathy; wtdPrP, white-tailed deer prion protein

■ REFERENCES

- (1) Belay, E. D.; Maddox, R. A.; Williams, E. S.; Miller, M. W.; Gambetti, P.; Schonberger, L. B. Chronic wasting disease and potential transmission to humans. *Emerging Infect. Dis.* **2004**, *10*, 977.
- (2) Haley, N. J.; Hoover, E. A. Chronic wasting disease of cervids: current knowledge and future perspectives. *Annu. Rev. Anim. Biosci.* **2015**, *3*, 305–325.
- (3) Williams, E. S.; Young, S. Chronic wasting disease of captive mule deer: A spongiform encephalopathy 1. *J. Wildl. Dis.* **1980**, *16*, 89–98.
- (4) Williams, E. S.; Young, S. Spongiform encephalopathy of rocky mountain elk 1. *J. Wildl. Dis.* **1982**, *18*, 465–471.
- (5) Spraker, T. R.; Miller, M. W.; Williams, E. S.; Getzy, D. M.; Adrian, W. J.; Schoonveld, G. G.; Spowart, R. A.; O'Rourke, K. I.; Miller, J. M.; Merz, P. A. Spongiform encephalopathy in free-ranging mule deer (*Odocoileus hemionus*), white-tailed deer (*Odocoileus virginianus*) and Rocky Mountain elk (*Cervus elaphus nelsoni*) in northcentral Colorado. *J. Wildl. Dis.* **1997**, *33*, 1–6.
- (6) Baeten, L. A.; Powers, B. E.; Jewell, J. E.; Spraker, T. R.; Miller, M. W. A natural case of chronic wasting disease in a free-ranging moose (*Alces alces shirasi*). *J. Wildl. Dis.* **2007**, *43*, 309–314.
- (7) Benestad, S. L.; Mitchell, G.; Simmons, M.; Ytrehus, B.; Vikoren, T. First case of chronic wasting disease in Europe in a Norwegian free-ranging reindeer. *Vet. Res.* **2016**, *47*, 88.

- (8) Benestad, S. L.; Telling, G. C. Chronic wasting disease: an evolving prion disease of cervids. *Handb. Clin. Neurol.* **2018**, *153*, 135–151.
- (9) Sohn, H.-J.; Jae-Hoon, K.; Jin-Ju, N.; Yi-Seok, J.; Young-Hwa, J.; Soo-Whan, A.; Ok-Kyung, K.; Dae-Yong, K.; BALACHANDRAN, A. A case of chronic wasting disease in an elk imported to Korea from Canada. *J. Vet. Med. Sci.* **2002**, *64*, 855–858.
- (10) Stokstad, E. Norway seeks to stamp out prion disease. *Science* **2017**, *356*, 12.
- (11) Gale, P.; Roberts, H. *Update on Chronic Wasting Disease in Europe*, 2018.
- (12) Pirisinu, L.; Tran, L.; Chiappini, B.; Vanni, I.; Di Bari, M. A.; Vaccari, G.; Vikøren, T.; Madslie, K. I.; Våge, J.; Spraker, T.; Mitchell, G.; Balachandran, A.; Baron, T.; Casalone, C.; Rolandsen, C. M.; Røed, K. H.; Agrimi, U.; Nonno, R.; Benestad, S. L. Novel Type of Chronic Wasting Disease Detected in Moose (*Alces alces*), Norway. *Emerging Infect. Dis.* **2018**, *24*, 2210–2218.
- (13) Imran, M.; Mahmood, S. An overview of animal prion diseases. *Virology* **2011**, *8*, 493.
- (14) Colby, D. W.; Prusiner, S. B. Prions. *Cold Spring Harbor Perspect. Biol.* **2011**, *3*, a006833.
- (15) Surewicz, W. K.; Apostol, M. I. Prion protein and its conformational conversion: a structural perspective. *Prion Proteins*; Springer, 2011; pp 135–167.
- (16) Riek, R.; Hornemann, S.; Wider, G.; Billeter, M.; Glockshuber, R.; Wüthrich, K. NMR structure of the mouse prion protein domain PrP (121–231). *Nature* **1996**, *382*, 180.
- (17) Biljan, I.; Ilc, G.; Plavec, J. Analysis of Prion Protein Structure Using Nuclear Magnetic Resonance Spectroscopy. *Prions Methods in Molecular Biology*; Springer, 2017; pp 35–49.
- (18) Williams, E. S. Chronic wasting disease. *Vet. Pathol.* **2005**, *42*, 530–549.
- (19) Miller, M. W.; Williams, E. S. Horizontal prion transmission in mule deer. *Nature* **2003**, *425*, 35–36.
- (20) Hill, A. F.; Collinge, J. Prion strains and species barriers. *Prions*; Karger Publishers, 2004; Vol. 11, pp 33–49.
- (21) Moore, R.-A.; Vorberg, I.; Priola, S.-A. Species barriers in prion diseases—brief review. *Infectious Diseases from Nature: Mechanisms of Viral Emergence and Persistence*; Springer, 2005; pp 187–202.
- (22) Kurt, T. D.; Jiang, L.; Fernández-Borges, N.; Bett, C.; Liu, J.; Yang, T.; Spraker, T. R.; Castilla, J.; Eisenberg, D.; Kong, Q.; Sigurdson, C. J. Human prion protein sequence elements impede cross-species chronic wasting disease transmission. *J. Clin. Invest.* **2015**, *125*, 1485–1496.
- (23) Sweeting, B.; Khan, M. Q.; Chakrabarty, A.; Pai, E. F. Structural factors underlying the species barrier and susceptibility to infection in prion disease. *Biochem. Cell Biol.* **2010**, *88*, 195–202.
- (24) Goldmann, W.; Hunter, N.; Smith, G.; Foster, J.; Hope, J. PrP genotype and agent effects in scrapie: change in allelic interaction with different isolates of agent in sheep, a natural host of scrapie. *J. Gen. Virol.* **1994**, *75*, 989–995.
- (25) Apetri, A. C.; Vanik, D. L.; Surewicz, W. K. Polymorphism at residue 129 modulates the conformational conversion of the D178N variant of human prion protein 90-231. *Biochemistry* **2005**, *44*, 15880–15888.
- (26) Palmer, M. S.; Dryden, A. J.; Hughes, J. T.; Collinge, J. Homozygous prion protein genotype predisposes to sporadic Creutzfeldt-Jakob disease. *Nature* **1991**, *352*, 340–342.
- (27) Fernández-Borges, N.; Espinosa, J. C.; Marín-Moreno, A.; Aguilar-Calvo, P.; Asante, E. A.; Kitamoto, T.; Mohri, S.; Andréoletti, O.; Torres, J. M. Protective Effect of Val129-PrP against Bovine Spongiform Encephalopathy but not Variant Creutzfeldt-Jakob Disease. *Emerging Infect. Dis.* **2017**, *23*, 1522–1530.
- (28) Robinson, S. J.; Samuel, M. D.; O'Rourke, K. I.; Johnson, C. J. The role of genetics in chronic wasting disease of North American cervids. *Prion* **2012**, *6*, 153–162.
- (29) Kelly, A. C.; Mateus-Pinilla, N. E.; Diffendorfer, J.; Jewell, E.; Ruiz, M. O.; Killefer, J.; Shelton, P.; Beissel, T.; Novakofski, J. Prion sequence polymorphisms and chronic wasting disease resistance in Illinois white-tailed deer (*Odocoileus virginianus*). *Prion* **2008**, *2*, 28–36.
- (30) Jewell, J. E.; Conner, M. M.; Wolfe, L. L.; Miller, M. W.; Williams, E. S. Low frequency of PrP genotype 225SF among free-ranging mule deer (*Odocoileus hemionus*) with chronic wasting disease. *J. Gen. Virol.* **2005**, *86*, 2127–2134.
- (31) O'Rourke, K. I.; Spraker, T. R.; Zhuang, D.; Greenlee, J. J.; Gidlewski, T. E.; Hamir, A. N. Elk with a long incubation prion disease phenotype have a unique PrPd profile. *NeuroReport* **2007**, *18*, 1935–1938.
- (32) Cervenáková, L.; Rohwer, R.; Williams, E. S.; Brown, P.; Gajdusek, D. C. High sequence homology of the PrP gene in mule deer and Rocky Mountain elk. *Lancet* **1997**, *350*, 219–220.
- (33) Perrott, M. R.; Sigurdson, C. J.; Mason, G. L.; Hoover, E. A. Evidence for distinct chronic wasting disease (CWD) strains in experimental CWD in ferrets. *J. Gen. Virol.* **2012**, *93*, 212–221.
- (34) Williams, E. S.; Young, S. Neuropathology of chronic wasting disease of mule deer (*Odocoileus hemionus*) and elk (*Cervus elaphus nelsoni*). *Vet. Pathol.* **1993**, *30*, 36–45.
- (35) Bian, J.; Christiansen, J. R.; Moreno, J. A.; Kane, S. J.; Khaychuk, V.; Gallegos, J.; Kim, S.; Telling, G. C. Primary structural differences at residue 226 of deer and elk PrP dictate selection of distinct CWD prion strains in gene-targeted mice. *Proc. Natl. Acad. Sci. U.S.A.* **2019**, *116*, 12478.
- (36) Baral, P. K.; Swayampakula, M.; Aguzzi, A.; James, M. N. G. X-ray structural and molecular dynamical studies of the globular domains of cow, deer, elk and Syrian hamster prion proteins. *J. Struct. Biol.* **2015**, *192*, 37–47.
- (37) Gossert, A. D.; Bonjour, S.; Lysek, D. A.; Fiorito, F.; Wüthrich, K. Prion protein NMR structures of elk and of mouse/elk hybrids. *Proc. Natl. Acad. Sci. U.S.A.* **2005**, *102*, 646–650.
- (38) Angers, R. C.; Kang, H.-E.; Napier, D.; Browning, S.; Seward, T.; Mathiason, C.; Balachandran, A.; McKenzie, D.; Castilla, J.; Soto, C.; Jewell, J.; Graham, C.; Hoover, E. A.; Telling, G. C. Prion strain mutation determined by prion protein conformational compatibility and primary structure. *Science* **2010**, *328*, 1154–1158.
- (39) Christen, B.; Hornemann, S.; Damberger, F. F.; Wüthrich, K. Prion protein NMR structure from tammar wallaby (*Macropus eugenii*) shows that the $\beta 2$ – $\alpha 2$ loop is modulated by long-range sequence effects. *J. Mol. Biol.* **2009**, *389*, 833–845.
- (40) Angers, R.; Christiansen, J.; Nalls, A. V.; Kang, H.-E.; Hunter, N.; Hoover, E.; Mathiason, C. K.; Sheetz, M.; Telling, G. C. Structural effects of PrP polymorphisms on intra- and interspecies prion transmission. *Proc. Natl. Acad. Sci. U.S.A.* **2014**, *111*, 11169–11174.
- (41) Kay, L. E.; Ikura, M.; Tschudin, R.; Bax, A. Three-dimensional triple-resonance NMR spectroscopy of isotopically enriched proteins. *J. Magn. Reson.* **1990**, *89*, 496–514.
- (42) Bax, A.; Grzesiek, S. Methodological advances in protein NMR. *NMR of Proteins*; Springer, 1993; pp 33–52.
- (43) Laskowski, R. A.; Rullmann, J. A. C.; MacArthur, M. W.; Kaptein, R.; Thornton, J. M. AQUA and PROCHECK-NMR: programs for checking the quality of protein structures solved by NMR. *J. Biomol. NMR* **1996**, *8*, 477–486.
- (44) Doreleijers, J. F.; Sousa da Silva, A. W.; Krieger, E.; Nabuurs, S. B.; Spronk, C. A. E. M.; Stevens, T. J.; Vranken, W. F.; Vriend, G.; Vuister, G. W. CING: an integrated residue-based structure validation program suite. *J. Biomol. NMR* **2012**, *54*, 267–283.
- (45) Bhattacharya, A.; Tejero, R.; Montelione, G. T. Evaluating protein structures determined by structural genomics consortia. *Proteins: Struct., Funct., Bioinf.* **2007**, *66*, 778–795.
- (46) Kumar, S.; Bansal, M. Geometrical and sequence characteristics of α -helices in globular proteins. *Biophys. J.* **1998**, *75*, 1935–1944.
- (47) Bansal, M.; Kumart, S.; Velavan, R. HELANAL: a program to characterize helix geometry in proteins. *J. Biomol. Struct. Dyn.* **2000**, *17*, 811–819.
- (48) Van der Kamp, M. W.; Daggett, V. Influence of pH on the human prion protein: insights into the early steps of misfolding. *Biophys. J.* **2010**, *99*, 2289–2298.

- (49) Fraczekiewicz, R.; Braun, W. Exact and efficient analytical calculation of the accessible surface areas and their gradients for macromolecules. *J. Comput. Chem.* **1998**, *19*, 319–333.
- (50) Sridharan, S.; Nicholls, A.; Sharp, K. A. A rapid method for calculating derivatives of solvent accessible surface areas of molecules. *J. Comput. Chem.* **1995**, *16*, 1038–1044.
- (51) Vaske, J. J.; Miller, C. A.; Ashbrook, A. L.; Needham, M. D. Proximity to chronic wasting disease, perceived risk, and social trust in the managing agency. *Hum. Dimens. Wildl.* **2018**, *23*, 115–128.
- (52) Hannaoui, S.; Schatzl, H. M.; Gilch, S. Chronic wasting disease: Emerging prions and their potential risk. *PLoS Pathog.* **2017**, *13*, No. e1006619.
- (53) Waddell, L.; Greig, J.; Mascarenhas, M.; Otten, A.; Corrin, T.; Hierlihy, K. Current evidence on the transmissibility of chronic wasting disease prions to humans—a systematic review. *Transboundary Emerging Dis.* **2018**, *65*, 37–49.
- (54) Sutherland, W. J.; Butchart, S. H. M.; Connor, B.; Culshaw, C.; Dicks, L. V.; Dinsdale, J.; Doran, H.; Entwistle, A. C.; Fleishman, E.; Gibbons, D. W.; Jiang, Z.; Keim, B.; Roux, X. L.; Lickorish, F. A.; Markillie, P.; Monk, K. A.; Mortimer, D.; Pearce-Higgins, J. W.; Peck, L. S.; Pretty, J.; Seymour, C. L.; Spalding, M. D.; Tonneijck, F. H.; Gleave, R. A. A 2018 Horizon Scan of Emerging Issues for Global Conservation and Biological Diversity. *Trends Ecol. Evol.* **2018**, *33*, 47–58.
- (55) Paramithiotis, E.; Pinard, M.; Lawton, T.; LaBoissiere, S.; Leathers, V. L.; Zou, W.-Q.; Estey, L. A.; Lamontagne, J.; Lehto, M. T.; Kondejewski, L. H.; Francoeur, G. P.; Papadopoulos, M.; Haghighat, A.; Spatz, S. J.; Head, M.; Will, R.; Ironside, J.; O'Rourke, K.; Tonelli, Q.; Ledebur, H. C.; Chakrabarty, A.; Cashman, N. R. A prion protein epitope selective for the pathologically misfolded conformation. *Nat. Med.* **2003**, *9*, 893.
- (56) Bett, C.; Fernández-Borges, N.; Kurt, T. D.; Lucero, M.; Nilsson, K. P. R.; Castilla, J.; Sigurdson, C. J. Structure of the β 2- α 2 loop and interspecies prion transmission. *FASEB J.* **2012**, *26*, 2868–2876.
- (57) Kurt, T. D.; Bett, C.; Fernández-Borges, N.; Joshi-Barr, S.; Hornemann, S.; Rülcke, T.; Castilla, J.; Wüthrich, K.; Aguzzi, A.; Sigurdson, C. J. Prion transmission prevented by modifying the β 2- α 2 loop structure of host PrPC. *J. Neurosci.* **2014**, *34*, 1022–1027.
- (58) Sigurdson, C. J.; Nilsson, K. P. R.; Hornemann, S.; Manco, G.; Fernández-Borges, N.; Schwarz, P.; Castilla, J.; Wüthrich, K.; Aguzzi, A. A molecular switch controls interspecies prion disease transmission in mice. *J. Clin. Invest.* **2010**, *120*, 2590.
- (59) Kurt, T. D.; Aguilar-Calvo, P.; Jiang, L.; Rodriguez, J. A.; Alderson, N.; Eisenberg, D. S.; Sigurdson, C. J. Asparagine and glutamine ladders promote cross-species prion conversion. *J. Biol. Chem.* **2017**, *292*, 19076–19086.
- (60) Caldarulo, E.; Barducci, A.; Wüthrich, K.; Parrinello, M. Prion protein β 2- α 2 loop conformational landscape. *Proc. Natl. Acad. Sci. U.S.A.* **2017**, *114*, 9617–9622.
- (61) Piening, N.; Nonno, R.; Di Bari, M.; Walter, S.; Windl, O.; Agrimi, U.; Kretzschmar, H. A.; Bertsch, U. Conversion efficiency of bank vole prion protein in vitro is determined by residues 155 and 170, but does not correlate with the high susceptibility of bank voles to sheep scrapie in vivo. *J. Biol. Chem.* **2006**, *281*, 9373–9384.
- (62) Scott, M.; Groth, D.; Foster, D.; Torchia, M.; Yang, S.-L.; DeArmond, S. J.; Prusiner, S. B. Propagation of prions with artificial properties in transgenic mice expressing chimeric PrP genes. *Cell* **1993**, *73*, 979–988.
- (63) Avbelj, M.; Hafner-Bratkovič, I.; Jerala, R. Introduction of glutamines into the B2–H2 loop promotes prion protein conversion. *Biochem. Biophys. Res. Commun.* **2011**, *413*, 521–526.
- (64) Kurt, T. D.; Jiang, L.; Bett, C.; Eisenberg, D.; Sigurdson, C. J. A proposed mechanism for the promotion of prion conversion involving a strictly conserved tyrosine residue in the β 2- α 2 loop of PrPC. *J. Biol. Chem.* **2014**, *289*, 10660–10667.
- (65) Eghiaian, F.; Daubenfeld, T.; Quenet, Y.; Van Audenhaege, M.; Bouin, A.-P.; Van Der Rest, G.; Grosclaude, J.; Rezaei, H. Diversity in prion protein oligomerization pathways results from domain expansion as revealed by hydrogen/deuterium exchange and disulfide linkage. *Proc. Natl. Acad. Sci. U.S.A.* **2007**, *104*, 7414–7419.
- (66) Singh, J.; Udgaonkar, J. B. Structural effects of multiple pathogenic mutations suggest a model for the initiation of misfolding of the prion protein. *Angew. Chem., Int. Ed. Engl.* **2015**, *54*, 7529–7533.
- (67) Miller, M. B.; Wang, D. W.; Wang, F.; Noble, G. P.; Ma, J.; Woods, V. L., Jr; Li, S.; Supattapone, S. Cofactor molecules induce structural transformation during infectious prion formation. *Structure* **2013**, *21*, 2061–2068.
- (68) Singh, J.; Kumar, H.; Sabareesan, A. T.; Udgaonkar, J. B. Rational stabilization of helix 2 of the prion protein prevents its misfolding and oligomerization. *J. Am. Chem. Soc.* **2014**, *136*, 16704–16707.
- (69) Brayton, K. A.; O'Rourke, K. I.; Lyda, A. K.; Miller, M. W.; Knowles, D. P. A processed pseudogene contributes to apparent mule deer prion gene heterogeneity. *Gene* **2004**, *326*, 167–173.
- (70) O'Rourke, K. I.; Spraker, T. R.; Hamburg, L. K.; Besser, T. E.; Brayton, K. A.; Knowles, D. P. Polymorphisms in the prion precursor functional gene but not the pseudogene are associated with susceptibility to chronic wasting disease in white-tailed deer. *J. Gen. Virol.* **2004**, *85*, 1339–1346.
- (71) Angers, R. C.; Seward, T. S.; Napier, D.; Green, M.; Hoover, E.; Spraker, T.; O'Rourke, K.; Balachandran, A.; Telling, G. C. Chronic wasting disease prions in elk antler velvet. *Emerging Infect. Dis.* **2009**, *15*, 696.
- (72) Pérez, D. R.; Damberger, F. F.; Wüthrich, K. Horse prion protein NMR structure and comparisons with related variants of the mouse prion protein. *J. Mol. Biol.* **2010**, *400*, 121–128.
- (73) Moreno, J. A.; Telling, G. C. Insights into mechanisms of transmission and pathogenesis from transgenic mouse models of prion diseases. *Prions*; Springer, 2017; pp 219–252.
- (74) Green, K. M.; Browning, S. R.; Seward, T. S.; Jewell, J. E.; Ross, D. L.; Green, M. A.; Williams, E. S.; Hoover, E. A.; Telling, G. C. The elk PRNP codon 132 polymorphism controls cervid and scrapie prion propagation. *J. Gen. Virol.* **2008**, *89*, 598–608.
- (75) Tropea, J. E.; Cherry, S.; Waugh, D. S. Expression and purification of soluble His 6-tagged TEV protease. *High throughput Protein Expression and Purification*; Springer, 2009; pp 297–307.
- (76) Güntert, P. Automated NMR structure calculation with CYANA. *Methods Mol. Biol.* **2004**, *278*, 353–378.
- (77) Krieger, E.; Koraimann, G.; Vriend, G. Increasing the precision of comparative models with YASARA NOVA—a self-parameterizing force field. *Proteins: Struct., Funct., Bioinf.* **2002**, *47*, 393–402.
- (78) Kay, L. E.; Torchia, D. A.; Bax, A. Backbone dynamics of proteins as studied by nitrogen-15 inverse detected heteronuclear NMR spectroscopy: application to staphylococcal nuclease. *Biochemistry* **1989**, *28*, 8972–8979.
- (79) Delaglio, F.; Grzesiek, S.; Vuister, G. W.; Zhu, G.; Pfeifer, J.; Bax, A. NMRPipe: a multidimensional spectral processing system based on UNIX pipes. *J. Biomol. NMR* **1995**, *6*, 277–293.
- (80) Keller, R. L. J. *The Computer Aided Resonance Assignment Tutorial*; CANTINA Verlag, 2004.
- (81) Goddard, K. D. SPARKY 3; University of California: San Francisco, 2008.
- (82) Shen, Y.; Delaglio, F.; Cornilescu, G.; Bax, A. TALOS+: a hybrid method for predicting protein backbone torsion angles from NMR chemical shifts. *J. Biomol. NMR* **2009**, *44*, 213–223.
- (83) Sievers, F.; Wilm, A.; Dineen, D.; Gibson, T. J.; Karplus, K.; Li, W.; Lopez, R.; McWilliam, H.; Remmert, M.; Söding, J.; Thompson, J. D.; Higgins, D. G. Fast, scalable generation of high-quality protein multiple sequence alignments using Clustal Omega. *Mol. Syst. Biol.* **2011**, *7*, 539.
- (84) Dolinsky, T. J.; Nielsen, J. E.; McCammon, J. A.; Baker, N. A. PDB2PQR: an automated pipeline for the setup of Poisson–Boltzmann electrostatics calculations. *Nucleic Acids Res.* **2004**, *32*, W665–W667.

(85) Baker, N. A.; Sept, D.; Joseph, S.; Holst, M. J.; McCammon, J. A. Electrostatics of nanosystems: application to microtubules and the ribosome. *Proc. Natl. Acad. Sci. U.S.A.* **2001**, *98*, 10037–10041.

(86) Søndergaard, C. R.; Olsson, M. H.; Rostkowski, M.; Jensen, J. H. Improved treatment of ligands and coupling effects in empirical calculation and rationalization of p K a values. *J. Chem. Theory Comput.* **2011**, *7*, 2284–2295.

(87) Olsson, M. H. M.; Søndergaard, C. R.; Rostkowski, M.; Jensen, J. H. PROPKA3: consistent treatment of internal and surface residues in empirical p K a predictions. *J. Chem. Theory Comput.* **2011**, *7*, 525–537.